nature communications

Article

https://doi.org/10.1038/s41467-025-58470-6

All-site alloyed perovskite for efficient and bright blue light-emitting diodes

Received: 17 December 2024

Accepted: 24 March 2025

Published online: 05 April 2025

Check for updates

Yu Chen[1], Ruishan Wang[1], Gunnar Kusch[2], Bo Xu[1], Chenjie Hao[1], Chen Xue[1], Lu Cheng[3], Lin Zhu[1], Jingmin Wang[1], Hai Li[1], Rachel A. Oliver[2], Nana Wang[1] ✉, Wei Huang[1,4,5] ✉ & Jianpu Wang[1,6] ✉

Perovskite light-emitting diodes have drawn great attention in the fields of displays and lighting, especially for applications requiring high efficiency and high brightness. While three-dimensional perovskite light-emitting diodes hold promise for achieving higher brightness compared to low-dimensional counterparts, efficient blue three-dimensional perovskite light-emitting diodes have remained a challenge due to defect formation during the disordered crystallization of multiple A-cation perovskite. Here we demonstrate an all-site alloy method that enables sequential A-site doping growth of formamidinium and cesium hybrid perovskite. This approach significantly reduces the trap density of the perovskite film by approximately one order of magnitude. Consequently, we achieve efficient and bright blue perovskite light-emitting diode with an external quantum efficiency of 23.3%, a luminous efficacy of 33.4 lm W^{-1}, and a luminance of approximately 5700 cd m^{-2} for the emission with a peak at 487 nm. This work provides a strategy for growing high-quality multicomponent perovskite for optoelectronics.

Solution-processed thin-film perovskite light-emitting diodes (LEDs) are considered to be promising candidates for emerging light-emitting technology owing to their high brightness, low power consumption, and potential low cost[1,2]. In recent years, significant advancements have been made in red and green perovskite LEDs, with their external quantum efficiencies (EQEs) approaching those of organic LEDs and quantum-dot LEDs[2–5]. However, the efficiency and brightness of blue perovskite LEDs have lagged behind, becoming an obstacle for their application in full-color displays. Mixed bromide/chloride (Br/Cl) three-dimensional (3D) perovskites with the ABX_3 formula exhibit high charge mobility and a high Auger recombination threshold, showing great promise for achieving efficient and bright blue LEDs[6,7]. To enhance the stability of the crystal structure and improve halide homogeneity in X-site alloyed perovskites, multiple A-site cations like formamidinium/cesium/rubidium (FA/Cs/Rb) have been widely utilized[8,9]. However, the competitive crystallization process of multiple A-site perovskite phases can lead to disordered growth and cation segregation[10,11], resulting in the formation of numerous defects. Here we demonstrate that the trap density in blue 3D perovskite can be significantly reduced by introducing a B-site alloy (lead/strontium, Pb/Sr) to facilitate a sequential A-site doping growth of perovskite. Based on these high-quality all-site alloyed perovskites, we demonstrate efficient and bright blue perovskite LEDs.

[1]State Key Laboratory of Flexible Electronics (LoFE) & Institute of Advanced Materials (IAM), School of Flexible Electronics (Future Technologies), Nanjing Tech University (NanjingTech), Nanjing 211816, China. [2]Department of Materials Science and Metallurgy, University of Cambridge, 27 Charles Babbage Road, Cambridge CB3 0FS, UK. [3]School of Microelectronics & Data Science, Anhui University of Technology, Ma'anshan 243002, China. [4]Shaanxi Institute of Flexible Electronics (SIFE), Xi'an Institute of Biomedical Materials & Engineering (IBME), Northwestern Polytechnical University (NPU), 127 West Youyi Road, Xi'an 710072, China. [5]Strait Laboratory of Flexible Electronics (SLoFE), Fujian Normal University, Fuzhou 350117, China. [6]The Materials and Electronics Research Center (MERC), School of Materials Science and Engineering and School of Microelectronics and Control Engineering, Changzhou University, Changzhou 213164, China. ✉e-mail: iamnnwang@njtech.edu.cn; vc@nwpu.edu.cn; iamjpwang@njtech.edu.cn

Results

High-performance perovskite films and light-emitting diodes

The all-site alloyed (FA/Cs/Rb)(Pb/Sr)(Br/Cl)$_3$ perovskite layers were prepared by spin-coating a precursor solution of formamidinium bromide (FABr), cesium bromide (CsBr), rubidium bromide (RbBr), lead chloride ($PbCl_2$), lead bromide ($PbBr_2$), strontium bromide ($SrBr_2$) and 2-(2-(2-aminoethoxy)ethoxy)acetic acid (AEAA) with a molar ratio of 0.2/1.2/0.1/0.56/0.44-x/x/0.2 dissolved in dimethyl sulfoxide (DMSO). We used Pb and Pb/Sr to denote perovskites prepared without and with 0.05 ratio $SrBr_2$, respectively. Both Pb and Pb/Sr films exhibit blue emission with a photoluminescence (PL) peak at 487 nm and similar absorption spectra (Supplementary Fig. 1). X-ray diffraction (XRD) data reveal typical diffraction peaks of 3D perovskite, with enhanced crystallinity observed in the Pb/Sr perovskite (Fig. 1a). These results indicate that the inclusion of small amount Sr^{2+} has a minimal effect on the crystal structure of the perovskite, unlike the introduction of a large amount of Sr^{2+}, which can enlarge the bandgap of perovskite[12–14]. Scanning electron microscope (SEM) images show that the Pb/Sr perovskite film possesses larger grains compared to the Pb film (Fig. 1b, c). It also exhibits a discrete morphology similar to the Pb perovskite sample, which is beneficial for light extraction in LEDs[15]. More importantly, the Pb/Sr perovskite exhibits an enhanced photoluminescence quantum efficiency (PLQE) of 75%, particularly at lower excitation intensities (Fig. 1d), suggesting reduced trap-assisted non-radiative recombination[16]. Transient PL decay measurements further demonstrate that the Pb/Sr perovskite exhibits a much longer PL lifetime compared to the Pb sample (Fig. 1e, f), confirming its lower trap density. By fitting the transient PL data, it is estimated that the trap density of the Pb/Sr sample is $4.2 \times 10^{14}\,cm^{-3}$, which is lower than in conventional blue perovskite films (approximately $10^{15}\,cm^{-3}$)[17] and almost one order of magnitude lower than the $2.2 \times 10^{15}\,cm^{-3}$ of the Pb perovskite film. The local properties of the perovskite films were investigated using cathodoluminescence (CL) measurements (Fig. 2), which can provide high-resolution information about the local emission behavior of perovskites[6,18]. The Pb perovskite film exhibits significant variation in the emission peak (Fig. 2e, g), with a high standard deviation (SD) of 1.9 nm. In contrast, the CL peak wavelength of the Pb/Sr perovskites is distributed much more narrowly (Fig. 2f, g), and the SD decreases to 1.5 nm, indicating improved uniformity of the perovskite grains.

We then fabricated blue LEDs using the above perovskite films (Fig. 3a). The device based on the Pb/Sr perovskite exhibits an electroluminescence (EL) peak at 487 nm (Fig. 3b), corresponding to Commission Internationale de l'Eclairage (CIE) coordinates of (0.070, 0.246) (Fig. 3c). The device demonstrates a low turn-on voltage of 2.4 V and reaches a maximum luminance of approximately 5700 cd m^{-2} (Fig. 3d). It achieves a peak EQE of 23.3% and a peak luminous efficacy of 33.4 lm W^{-1} (Fig. 3e), representing the most efficient blue 3D perovskite LED to date (Supplementary Table 1)[8,19]. These Pb/Sr perovskite devices exhibit an average peak EQE of 21.5% (Fig. 3f). The Pb/Sr perovskite LED reaches a longer half-lifetime of 42 min compared to the 11 min of the Pb perovskite device (Supplementary Fig. 2a). Additionally, the Pb/Sr LED exhibits good color stability, with spectra remaining unchanged after the stability measurement (Supplementary Fig. 2b). This improved stability can be attributed to the reduced trap density in the Pb/Sr perovskite film, which can mitigate ion migration[20]. Furthermore, by increasing the ratio of Cl to Br in the Pb/Sr perovskite through in situ halide exchange using a mixed tetraphenylphosphonium chloride (TPPC) and phenylbutylammonium chloride (PBAC) solution[21], the EL peak of the devices can be tuned to deep blue as 468 nm and 464 nm. The devices achieve high peak EQEs of 11.9% and 7.5%, and luminous efficacy of 7.3 and 3.9 lm W^{-1}, respectively. Importantly, the deep-blue device at 464 nm exhibits CIE coordinates of (0.132, 0.046), fully meeting the Rec. 2020 blue standard (0.131, 0.046). In contrast, deep-blue Pb perovskite LEDs with an EL peak at 464 nm can only achieve a low EQE of 2.1% (Supplementary Fig. 3), which is attributed to higher trap densities.

Formation mechanism of high-quality perovskites

To verify how B-site alloying enhances the quality of the perovskite film, we compared the PL spectra of samples during the spin-coating, vapor-assisted crystallization (VAC), and thermal annealing processes.

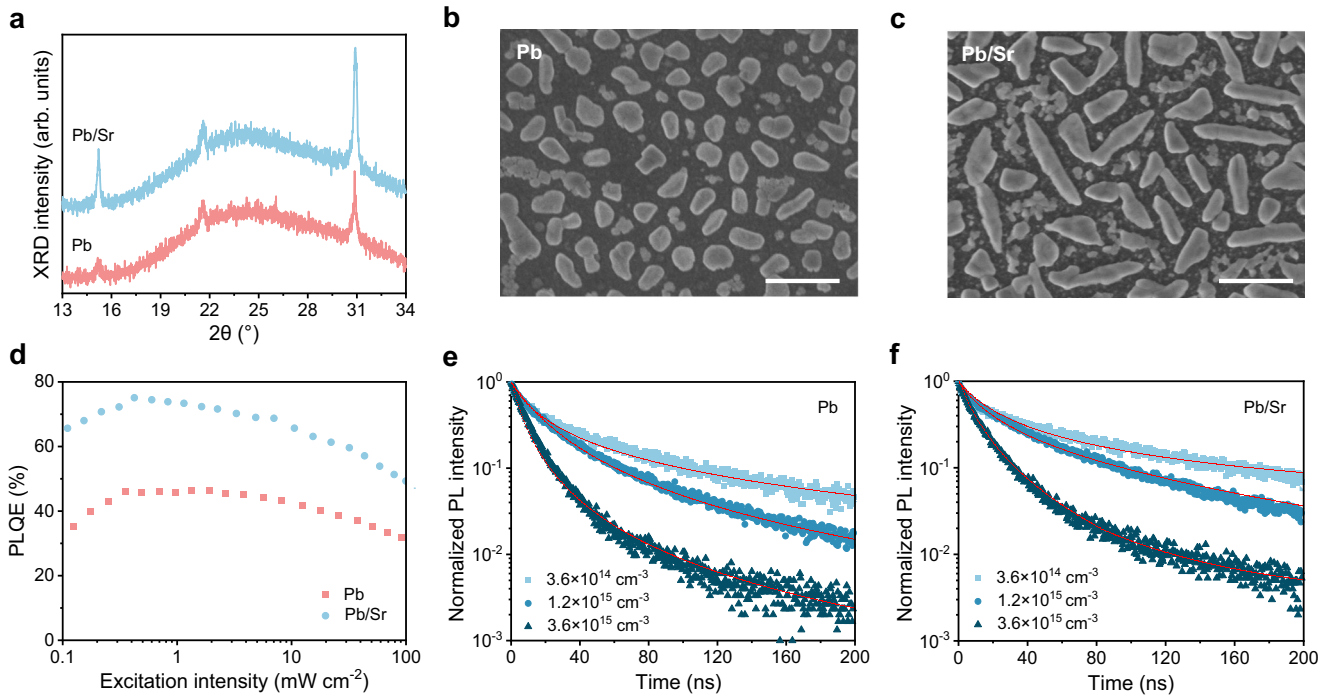

Fig. 1 | Characterizations of perovskite films. a XRD patterns. **b**, **c** SEM images of Pb (**b**) or Pb/Sr (**c**) perovskites. Scale bar, 500 nm. **d** Excitation-intensity-dependent PLQEs. **e**, **f** Transient PL decays of Pb (**e**) or Pb/Sr (**f**) perovskites.

https://doi.org/10.1038/s41467-025-58470-6

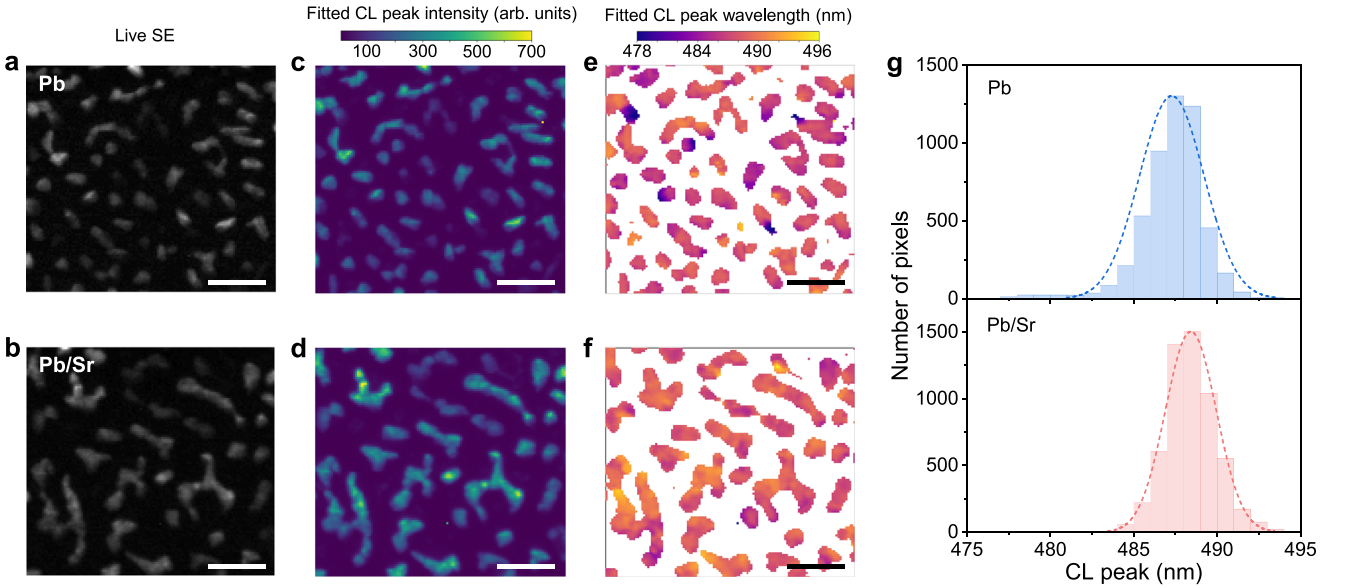

Fig. 2 | Local characterizations of Pb and Pb/Sr perovskite films. a, **b** SEM image of Pb (**a**) and Pb/Sr (**b**) perovskite films. **c**, **d** Corresponding CL peak intensity maps of Pb (**c**) and Pb/Sr (**d**) perovskite films. **e**, **f** CL peak wavelength maps of Pb (**e**) and Pb/Sr (**f**) perovskite films. Scale bar, 700 nm. **g** Statistics of CL peak in the measured Pb and Pb/Sr perovskite films. The SD values of the Pb and Pb/Sr samples are 1.9 nm and 1.5 nm, respectively.

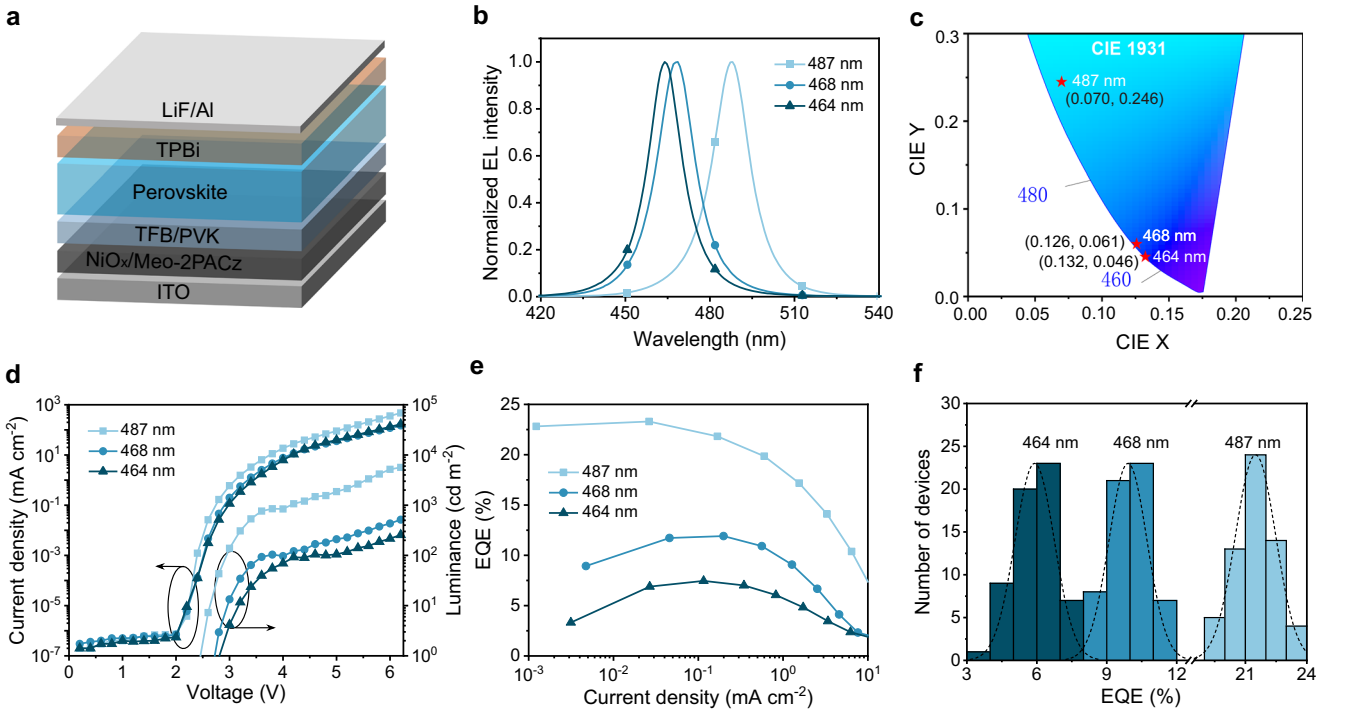

Fig. 3 | Device structure and characteristics of perovskite LEDs. a Schematic illustration of the device architecture. **b** EL spectra of devices. **c** CIE coordinates. **d** Current density and luminance versus voltage. **e** Dependence of the EQE on the current density. **f** Histograms of peak EQEs. Statistics of 60 devices with different emissions show average peak EQEs of 21.5%, 9.5%, and 5.5% with relative standard deviations of 4.6%, 8.3%, and 14.4%, respectively.

The results demonstrate that the Pb perovskite sample begins to form emitters approximately 35 s during the spin-coating process, exhibiting a PL peak at approximately 469 nm (Fig. 4a and Supplementary Fig. 4a). In contrast, the Pb/Sr sample shows no PL signal from the perovskite (Fig. 4b and Supplementary Fig. 4b), indicating that Sr doping can retard the crystallization of our perovskite. Then, during the dimethylformamide (DMF) vapor treatment process, both Pb and Pb/Sr samples exhibit enhanced and red-shifted PL spectra (Fig. 4c, d), which can be attributed to the growth of perovskite and the migration of Br^- to the Cl-rich perovskite with the assistance of DMF vapor[22]. During the subsequent thermal annealing process, the PL peak of the Pb sample remains constant at approximately 481 nm (Fig. 4e). In contrast, the PL peak of the Pb/Sr perovskite exhibits a blue shift from 487 nm to 481 nm within 5 s (Fig. 4f and Supplementary Fig. 4e). This observation indicates that the Pb/Sr perovskite experiences distinguishable growth during the annealing process, which is further confirmed by SEM images and XRD data of perovskite films annealed for various times. SEM measurements show that the as-prepared Pb/Sr

https://doi.org/10.1038/s41467-025-58470-6

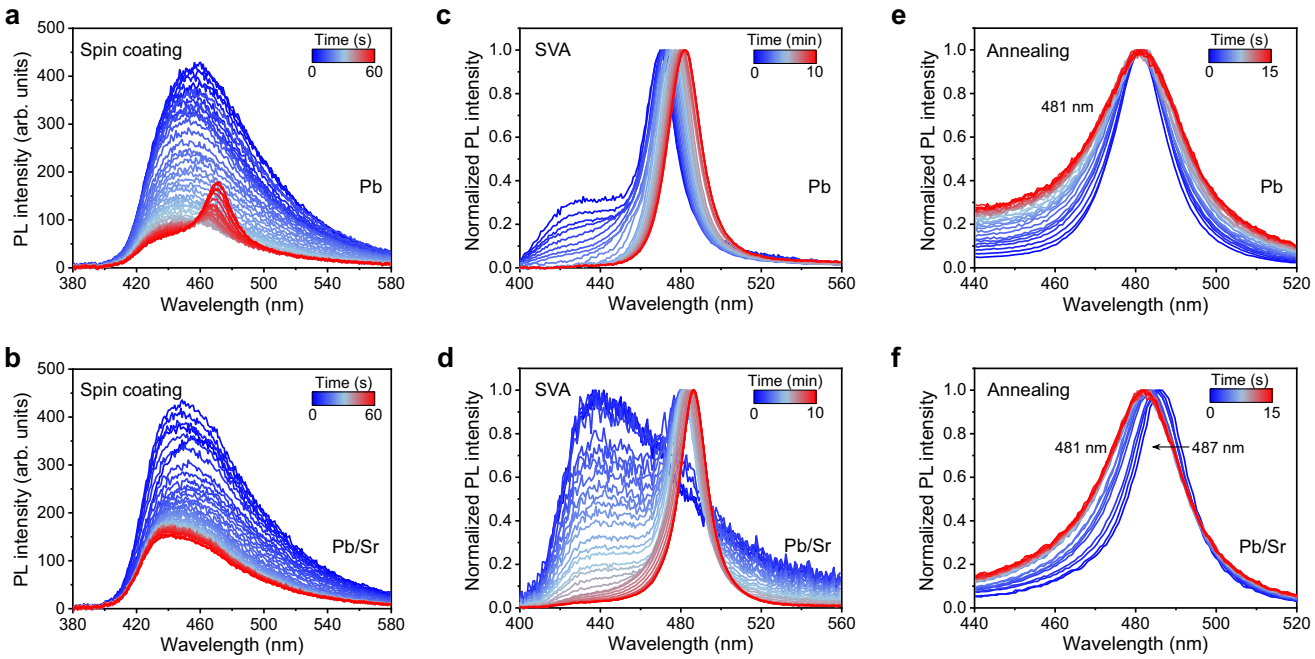

Fig. 4 | In situ PL measurements of perovskites during the growth process. **a**, **b** PL spectra of Pb (**a**) and Pb/Sr (**b**) perovskites during the spin-coating process. The broad emission between 420 nm and 500 nm are associated with TFB. The control sample exhibits the emission from perovskite after 35 s from the start of spin-coating. **c**, **d** Normalized PL spectra of Pb (**c**) and Pb/Sr (**d**) perovskites during the vapor-assisted crystallization process. **e**, **f** Normalized PL spectra of Pb (**e**) and Pb/Sr (**f**) perovskites during the initial 15 s annealing process. The PL peaks remain unchanged during the sequential annealing process.

sample consists of large grains embedded in some mud bank-like clusters (Supplementary Fig. 5a). As the annealing time increases, the mud bank-like clusters gradually grow and merge into large grains, and the XRD peak at 30.7° gradually shifts to a larger diffraction angle at 30.9°, accompanied by enhanced diffraction intensity (Supplementary Fig. 5c). This observation indicates that after introducing Sr, the perovskite experiences a significant evolution of two phases during the annealing process. In contrast, the Pb sample exhibits a similar morphology and XRD pattern during the annealing process (Supplementary Fig. 5b, d). Therefore, we conclude that while the crystallization of the Pb sample mainly occurs before the annealing process, the Pb/Sr perovskite experiences a slower, stepwise crystallization pathway, contributing to the high-quality perovskite.

We then investigate how the Sr-doping affects the crystallization of the perovskite. The elemental analysis using Auger electron spectroscopy (AES) measurements reveals a stronger carbon signal in the large grains of the as-prepared Pb/Sr sample without annealing, while the signal of Cs is higher in the mud bank-like clusters (Supplementary Fig. 5e). This finding suggests that the large and mud bank-like clusters correspond to emissive FA-rich perovskite phase and Cs-rich non-perovskite phase, respectively. After being annealed for 10 min, the grains exhibit similar C and Cs signals (Supplementary Fig. 5f). We infer that during the thermal annealing process, there exist cation exchanges between the FA-rich and Cs-rich phases, with Cs^+ migrating into the FA-rich perovskite framework to replace the FA^+ [23]. This leads to blue-shifted PL spectra and a shift of the XRD peak to a larger angle[24] (Fig. 4f and Supplementary Fig. 5c). Similar cation exchange processes are also observed in (FA/Cs/Rb)(Pb/Sr)Br_3 perovskite, further supporting this A-site doping growth process (Supplementary Fig. 6).

To reveal the origin of this unique crystallization pathway induced by Pb/Sr alloying, we conducted X-ray photoelectron spectroscopy (XPS) measurements. The results show that the $SrBr_2$ and CsBr sample exhibits a larger shift of the Sr *3d* peak towards a higher binding energy compared to the $SrBr_2$ + FABr sample (Supplementary Fig. 7a), which can be attributed to the stronger ionic bonds between Cs^+ and $[SrBr_3]^-$ (Supplementary Fig. 7b). Furthermore, theoretical simulations show that the average distance between Sr^{2+} and Cs^+ ions is 4.964 Å, while the distance between Sr^{2+} and FA^+ ions is 5.401 Å, with DMSO solvent molecules surrounding the cations (Supplementary Fig. 7c, d). This indicates that the interaction between $[SrBr_3]^-$ and Cs^+ is stronger than that between $[SrBr_3]^-$ and FA^+, which is consistent with the solid-state structures (average Cs-Sr distance: 2.904 Å and average FA-Sr distance: 3.960 Å) (Supplementary Fig. 7e, f). Consequently, we can conclude that the strong interaction between $SrBr_2$ and CsBr impedes the initial growth of mixed FA/Cs alloyed perovskite, leading to the growth of FA-rich perovskite. Additionally, the FA-rich perovskite can undergo oriented growth with the assistance of AEAA, resulting in ordered inorganic frameworks with low defects[25]. As the annealing time increases, Cs^+ gradually migrates into the ordered FA-rich perovskite framework, maintaining high-quality perovskite grains. This is further supported by the CL intensity map, which shows that the large grains in the Pb/Sr perovskite exhibit a much more uniform and higher CL intensity compared to the Pb sample (Fig. 2).

We believe that the above sequential A-site doping growth of FA/Cs hybrid perovskites plays a critical role in achieving low-defect perovskites and is the key for the impressive device performance, as the peak EQE of the Pb perovskite device is only 13.5% (Supplementary Fig. 8). As shown in Supplementary Fig. 8a, b, increasing the ratio of $SrBr_2$ gradually retards the growth of the FA/Cs perovskite while simultaneously increasing grain size and enhancing crystallinity. This results in a reduced defect density of the perovskite, leading to improved PLQEs (Supplementary Fig. 8c). When the $SrBr_2$ ratio is further increased to 0.07, the PLQE starts to reduce. Moreover, CL measurements indicate that a 0.1 ratio of $SrBr_2$ can result in heterogeneous emissions, wherein the perovskite grain edges exhibit a blue-shifted emission peak compared to the grain centers (Supplementary Fig. 8g–i). This can be attributed to the impeded migration of Cs^+ into the FA-rich perovskite framework at a higher $SrBr_2$ ratio.

Discussion

The A- and X-site alloyed perovskite strategy has been widely employed to achieve high-quality perovskite films, relying on precise

control of crystallization for multiple phases. However, effectively controlling the rapid and disordered crystallization of multi-component blue perovskites has remained a challenge. In our work, we demonstrate that the B-site Pb/Sr alloy can further reduce the defect density of blue perovskite films by forming an ordered stepwise crystallization of FA/Cs hybrid perovskites. Based on this all-site alloy strategy, we have achieved efficient and bright blue perovskite LEDs with a peak EQE of 23.3% and a peak luminous efficacy of 33.4 lm W^{-1}. Moreover, this strategy can be employed for deep-blue perovskites, enabling the fabrication of efficient deep-blue LEDs with high brightness. Our advances in crystallization control provide the guidelines for achieving high-performance multicomponent perovskites.

Methods

Synthesis and material preparation

The precursor solution of (FA/Cs/Rb)(Pb/Sr)(Br/Cl)$_3$ perovskite was prepared by dissolving FABr, CsBr, RbBr, $PbCl_2$, $PbBr_2$, $SrBr_2$, and AEAA with a molar ratio of 0.2/1.2/0.1/0.56/0.44-x/x/0.2 in DMSO. The solution was stirred at 60 °C overnight in a N_2-filed glovebox before use. The (FA/Cs/Rb)(Pb/Sr)Br_3 perovskite precursor solution was prepared by dissolving FABr, CsBr, RbBr, $PbBr_2$, $SrBr_2$, and AEAA with a molar ratio of 0.2/1.2/0.1/0.95/0.05/0.2 in DMSO.

Film and device fabrication

The devices have a structure of indium tin oxide (ITO)/nickel oxide (NiO_x):[2-(3,6-Dimethoxy-9H-carbazol-9-yl)ethyl]phosphonic Aicd (Meo-2PACz) (10 nm)/poly(9,9-dioctyl-fluorence-co-N-)4-butylphenyl) diphenylamine) (TFB):poly(9-vinylcarbazole) (PVK) (25 nm)/perovskite (around 50 nm)/2,2′,2″-(1,3,5-benzinetriyl)tris(1-phenyl-1H-benzimidazole) (TPBi; 50 nm)/lithium fluoride (LiF; 1.2 nm)/aluminum (Al; 100 nm). All devices were fabricated on ITO-coated glass substrates with a device area of 3 mm^2. NiO_x nanocrystals obtained from Avantama AG were spin-coated onto ITO glass at 4000 rpm for 30 s and annealed at 150 °C for 10 min. The NiO_x-coated substrates were then transferred to the N_2-filled glovebox. The Meo-2PACz layer, dissolved in isopropanol (IPA) at a concentration of 1 mg mL^{-1}, was spin-coated at 2000 rpm for 30 s and annealed at 100 °C for 10 min. The TFB layer, dissolved in m-xylene at a concentration of 5 mg mL^{-1}, was spin-coated at 2000 rpm for 45 s and annealed at 150 °C for 30 min. Next, the PVK layer, dissolved in chlorobenzene at a concentration of 3 mg mL^{-1}, was spin-coated at 2000 rpm for 30 s and annealed at 120 °C for 20 min. The perovskite layers were prepared by spin-coating the precursor solutions onto the PVK film at 5000 rpm for 45 s. Subsequently, the wet perovskite films were transferred into a petri dish containing 20 µL DMF to improve the homogeneity of halides[22]. After 10 min of DMF vapor treatment, all perovskite films were annealed at 90 °C for 10 min. For perovskite films with TPPC + PBAC treatments, post-treatment solutions with 2.7 × 10^{-3} mM TPPC + 5.4 × 10^{-3} mM PBAC and 3.2 × 10^{-3} mM TPPC + 6.5 × 10^{-3} mM PBAC were used to achieve devices with EL peaks of 468 nm and 464 nm, respectively. Finally, the TPBi, LiF, and Al layers were thermally evaporated onto the perovskite films.

Device characterization

All device measurements were performed in a nitrogen-filled glovebox using an integrated system comprising a Keithley 2400 source meter, a fiber integration sphere (FOIS-1), and a QE65 Pro spectrometer[26]. Photon collection was achieved directly through the integrating sphere and spectrometer. Current-voltage sweeps were conducted from zero bias to forward bias at a bias rate of 0.2 V s^{-1}. Stability measurements were carried out using a Keithley 2450 source meter, a Keithley 2000 electric-meter, and a Thorlabs PDA100A photodetector (Nanjing Ouyi Optoelectronics Technology) in a glovebox at room temperature[27].

Film characterization

XRD data were acquired using a RIGAKU SmartLab 3 kW X-ray diffractometer. SEM images were obtained with a JEOL5 JSM-7800F microscope. PL spectra were measured using a QE65 Pro spectrometer with a 375 nm CW laser as the excitation source. In situ PL spectra were collected using an ISAS-HI001 system (Nanjing Ouyi Optoelectronics Technology) equipped with a 375 nm CW laser[28]. PLQEs were determined using an integrating sphere system and a 375 nm CW laser[29]. Time-resolved PL measurements were performed with an Edinburgh Instrument (FLS980 spectrometer) and a 445 nm pulsed laser. AES data were collected using a PHI710 Auger Electron Spectrometer, with samples transferred into the AES chamber via a nitrogen-filled glovebox to avoid atmospheric exposure. XPS measurements were conducted using a Thermo Scientific ESCALAB Xi+ XPS microprobe with an Al Kα anode (E = 1486 eV). Cathodoluminescence hyperspectral mapping was performed using an Attolight Allalin 4027 Chronos dedicated CL-SEM. CL spectra were acquired with an acceleration energy of 3 keV, a beam current of 62 pA, and an iHR320 spectrometer equipped with a 150 l mm^{-1} grating blazed at 500 nm and an Andor 1024 px charged coupled device. Beam current calibration was performed using a Faraday cup prior to measurements. Electrospray ionization time-of-flight mass spectrometry (ESI-TOF-MS) was conducted using an Agilent 6230 TOF LC/MS.

Calculations

First-principles calculations were performed using density functional theory as implemented in the Vienna Ab initio Simulation package (VASP) with the projector-augmented wave method[30,31]. Exchange-correlation interactions were described by the generalized-gradient approximation with the Perdew-Burke-Ernzerhof (PBE) functional[32]. For electronic structure calculations, an energy cut-off of 400 eV was employed. The unit cell was constructed as a 10 × 10 × 10 supercell containing one $[SrBr_3]^-$ anion, one cation (Cs^+ or FA^+), and four DMSO solvent molecules to model the intermediate phase between the solution and solid phases. The unit cell was fully relaxed, and a 2 × 2 × 2 Monkhorst-Pack k-point grid was used for structural optimizations and switching pathways calculations[33]. Structural optimizations were considered complete when the root-mean-square forces were less than 0.01 eV/Å.

Data availability

The data that support the finding of this study are provided in the Source data file. Source data are provided with this paper.

References

1. Tan, Z.-K. et al. Bright light-emitting diodes based on organometal halide perovskite. *Nat. Nanotechnol.* **9**, 687–692 (2014).
2. Li, M. et al. Acceleration of radiative recombination for efficient perovskite LEDs. *Nature* **630**, 631–635 (2024).
3. Li, H. et al. Nanosurface-reconstructed perovskite for highly efficient and stable active-matrix light-emitting diode display. *Nat. Nanotechnol.* **19**, 638–645 (2024).
4. Ding, S. et al. Phase dimensions resolving of efficient and stable perovskite light-emitting diodes at high brightness. *Nat. Photonics* **18**, 363–370 (2024).
5. Wei, K. et al. Perovskite heteroepitaxy for high-efficiency and stable pure-red LEDs. *Nature* **638**, 949–956 (2025).
6. Cheng, L. et al. Halide homogenization for high-performance blue perovskite electroluminescence. *Research* **2020**, 9017871 (2020).
7. Lee, S. et al. Brightening deep-blue perovskite light-emitting diodes: a path to Rec. 2020. *Sci. Adv.* **10**, eadn8465 (2024).
8. Xiong, W. et al. Efficient and bright blue perovskite LEDs enabled by a carbazole-phosphonic acid interface. *ACS Energy Lett.* **8**, 2897–2903 (2023).

9. Luo, X. et al. Effects of local compositional heterogeneity in mixed halide perovskites on blue electroluminescence. *Matter* **7**, 1054–1070 (2024).
10. Kubicki, D. J. et al. Phase segregation in Cs-, Rb- and K-doped mixed-cation $(MA)_x(FA)_{1-x}PbI_3$ hybrid perovskites from solid-state NMR. *J. Am. Chem. Soc.* **139**, 14173–14180 (2017).
11. Qin, M. et al. Precise control of perovskite crystallization kinetics via sequential A-site doping. *Adv. Mater.* **32**, 2004630 (2020).
12. Cai, L. et al. Efficient and bright pure-blue all-inorganic perovskite light-emitting diodes from an ecofriendly alloy. *J. Phys. Chem. Lett.* **12**, 1747–1753 (2021).
13. Li, J. et al. Strontium ion B-site substitution for spectral-stable blue emitting perovskite light-emitting diodes. *Adv. Opt. Mater.* **8**, 2001073 (2020).
14. Li, J. et al. Hole transport layer modification for highly efficient divalent ion-doped pure blue perovskite light-emitting diodes. *Adv. Opt. Mater.* **11**, 2201883 (2023).
15. Cao, Y. et al. Perovskite light-emitting diodes based on spontaneously formed submicrometre-scale structures. *Nature* **562**, 249–253 (2018).
16. Deschler, F. et al. High photoluminescence efficiency and optically pumped lasing in solution-processed mixed halide perovskite semiconductors. *J. Phys. Chem. Lett.* **5**, 1421–1426 (2014).
17. Jiang, Y. et al. Synthesis-on-substrate of quantum dot solids. *Nature* **612**, 679–684 (2022).
18. Yacobi, B. G. & Holt, D. B. Cathodoluminescence scanning electron microscopy of semiconductors. *J. Appl. Phys.* **59**, R1–R24 (1986).
19. Liu, A. et al. Optimizing perovskite surfaces to enhance post-treatment for efficient blue mixed-halide perovskite light-emitting diodes. *Adv. Mater.* 2414788 https://doi.org/10.1002/adma.202414788 (2024).
20. Wang, X. et al. Specific influences of trap states with distinct spatial and energetic distributions on ion migration dynamics in metal halide perovskites. *Nano Lett.* **24**, 16443–16449 (2024).
21. Tong, Y. et al. In situ halide exchange of cesium lead halide perovskites for blue light-emitting diodes. *Adv. Mater.* **35**, 2207111 (2023).
22. Karlsson, M. et al. Mixed halide perovskites for spectrally stable and high-efficiency blue light-emitting diodes. *Nat. Commun.* **12**, 361 (2021).
23. Wang, X. et al. Stable cesium-rich formamidinium/cesium pure-iodide perovskites for efficient photovoltaics. *ACS Energy Lett.* **6**, 2735–2741 (2021).
24. Yuan, F. et al. A cocktail of multiple cations in inorganic halide perovskite toward efficient and highly stable blue light-emitting diodes. *ACS Energy Lett.* **5**, 1062–1069 (2020).
25. Zhu, L. et al. Unveiling the additive-assisted oriented growth of perovskite crystallite for high performance light-emitting diodes. *Nat. Commun.* **12**, 5081 (2021).
26. Wang, N. et al. Perovskite light-emitting diodes based on solution-processed self-organized multiple quantum wells. *Nat. Photonics* **10**, 699–704 (2016).
27. Yi, C. et al. Elevating charge transport layer for stable perovskite light-emitting diodes. *Adv. Mater.* **36**, 2400658 (2024).
28. Min, H. et al. Additive treatment yields high-performance lead-free perovskite light-emitting diodes. *Nat. Photonics* **17**, 755–760 (2023).
29. de Mello, J. C., Wittmann, H. F. & Friend, R. H. An improved experimental determination of external photoluminescence quantum efficiency. *Adv. Mater.* **9**, 230–232 (1997).
30. Kresse, G. & Hafner, J. Ab initio molecular dynamics for liquid metals. *Phys. Rev. B* **47**, 558–561 (1993).
31. Blöchl, P. E. Projector augmented-wave method. *Phys. Rev. B* **50**, 17953–17979 (1994).
32. Perdew, J. P., Burke, K. & Ernzerhof, M. Generalized gradient approximation made simple. *Phys. Rev. Lett.* **77**, 3865–3868 (1996).
33. Monkhorst, H. J. & Pack, J. D. Special points for Brillouin-zone integrations. *Phys. Rev. B* **13**, 5188–5192 (1976).

Acknowledgements

This work is financially supported by the National Key Research and Development Program of China (2022YFA1204800, Jianpu Wang; 2023YFB3608900, N.W.), the National Natural Science Foundation of China (52233011, Jianpu Wang; 62288102, W.H.; 62375124, N.W.), the Natural Science Foundation of Jiangsu Province, China (BK20240002, N.W.). The authors are grateful for the technical support for Nano-X from Suzhou Institute of Nano-Tech and Nano-Bionics, Chinese Academy of Sciences (SINANO). CL studies used equipment supported by the EPSRC under grant number EP/R025193/1 (R.A.O.).

Author contributions

Jianpu Wang, N.W. and W.H. conceived the project. N.W. and Jianpu Wang designed the experiments. Y.C. carried out device design, fabrication and characterizations with the assistance of R.W. and B.X. C.H. characterized the trap densities of perovskite films. G.K. performed CL measurement and data processing under the supervision of R.A.O. Y.C. carried out the optical characterizations of perovskite films with the assistance of B.X., L.C. and Jingmin Wang. C.X. and L.Z. conducted the analysis of the interaction between CsBr and $SrBr_2$. N.W. wrote the first draft of the manuscript. Jianpu Wang, H.L. and W.H. provided major revisions.

Competing interests

The authors declare no competing interests.

Additional information

Supplementary information The online version contains supplementary material available at https://doi.org/10.1038/s41467-025-58470-6.

Correspondence and requests for materials should be addressed to Nana Wang, Wei Huang or Jianpu Wang.

Peer review information *Nature Communications* thanks the anonymous reviewer(s) for their contribution to the peer review of this work. A peer review file is available.